Optical Properties of Highly Conductive SrMoO$_3$ Oxide Thin Films in the THz Band and Beyond

Stefan Regensburger[1] ⓘ · Mahdad Mohammadi[2] · Arslan A. Khawaja[1] ·
Aldin Radetinac[2] · Philipp Komissinskiy[2] ⓘ · Lambert Alff[2] ⓘ · Sascha Preu[1] ⓘ

© The Author(s) 2020

Abstract

Strontium molybdate (SrMoO$_3$) thin films are grown epitaxially by pulsed laser deposition onto gadolinium scandate (GdScO$_3$) substrates and characterized in the terahertz (THz) and visible part of the electromagnetic spectrum. X-ray diffraction measurements prove a high crystallinity and phase-pure growth of the thin films. The high-quality SrMoO$_3$ thin films feature a room temperature DC conductivity of around $3\frac{1}{\mu\Omega m}$. SrMoO$_3$ is characterized in the THz frequency range by time domain spectroscopy. The resulting AC conductivity is in excellent agreement with the DC value. A Lorentz-Drude oscillator approach models the THz and visible conductivity of SrMoO$_3$ very well. We compare the results of the SrMoO$_3$ thin films to a standard, sputtered gold film, with a resulting THz conductivity of $8\frac{1}{\mu\Omega m}$. The comparison demonstrates that oxide thin film–based devices can play an important role in future THz technology.

Keywords SrMoO$_3$ · GdScO$_3$ · Perovskite · Conductive thin film · THz spectroscopy

1 Introduction

The vast variety of functional properties make the material class of perovskite oxides and related structures predestined for realization of all-oxide epitaxial metal-insulator-metal (MIM) heterostructures in high-frequency microelectronic devices.

✉ Stefan Regensburger
stefan.regensburger@tu-darmstadt.de

1 THz Devices and Systems, Technische Universität Darmstadt, Darmstadt, Germany

2 Institute of Materials Science, Technische Universität Darmstadt, Darmstadt, Germany

The epitaxial nature of such heterostructures allows lower defect densities and there-fore enhanced functional properties in comparison with polycrystalline thin films. Interface engineering at the atomic level and precise stoichiometry tuning of the layers in MIM varactor heterostructures enable improved functional properties of the materials such as high electric conductivity of oxide electrodes and high tun-ability of the dielectrics [1, 2]. Moreover, all-oxide epitaxial MIM heterostructures, including structurally compatible high-temperature superconductors, can be used for realization of novel thermally tuned THz metamaterials [3, 4].

For all-oxide MIM heterostructures, the cubic perovskite oxide $SrMoO_3$ (SMO) is the material with the highest conductivity of any perovskite reported so far [1, 5]. The partially reduced Mo^{4+} B-site cation provides a high concentration of charge carriers in the material, resulting in a room temperature conductivity of $20\frac{1}{\mu\Omega m}$ for an SMO single crystal [6]. This value surpasses even conventional electrode metals like platinum. So far, SMO thin films have been characterized in the DC, microwave, and visible frequency range [5, 7, 8]. Measurements of the specific heat indicate an increased effective mass of $m_e^* = 2.0 \ldots 2.6 \, m_b$ in comparison with the values from band theory, m_b [9, 10]. The increased m_e^* in combination with the high elec-trical conductivity makes SMO an interesting candidate for application in plasmonic devices or transparent conductors [8, 11].

This paper aims at the characterization of SMO conductivity in the yet unexplored THz range up to the visible electromagnetic spectrum in order to facilitate novel THz devices based on perovskite oxide thin film heterostructures. For that purpose, high-quality, single-crystalline SMO epitaxial thin films are deposited onto $GdScO_3$ substrates (GSO) by pulsed laser deposition. We measure the AC conductivity of the SMO films in the THz and visible domain and compare it to literature values for the microwave frequency range. Furthermore, we compare the AC conductivity of the SMO thin film to the AC conductivity of a sputtered gold film.

2 Theoretical Background

The AC conductivity of the thin films is characterized in a THz transmission config-uration. Dividing the electrical field transmitted through the thin film and substrate E_{fs} by the electrical field transmitted through the substrate E_s yields the film trans-mission $t = E_{fs}/E_s$. Attenuation and time delay of the electrical field result in a complex relative transmission t. The AC conductivity σ of a highly conductive thin film on an interface between air and a substrate can be extracted using Tinkham's formula [12–14] from the film transmission, t, with a substrate with refractive index of n_{GSO}, yielding

$$\sigma = \frac{n_{GSO} + 1}{Z_0 d} \left(\frac{1}{t} + 1 \right), \tag{1}$$

where Z_0 is the free-space impedance and d the thickness of the thin film. In the THz-domain, the simple Drude model can describe most features of conductors [13, 14]. The THz conductivity of SMO can also be described by the simple Drude model:

$$\sigma = \frac{\epsilon_0 \omega_{p0}^2 \tau_0}{1 - i \tau_0 \omega}. \tag{2}$$

For taking both optical and THz data into account, a single oscillator at DC, however, is usually insufficient. Therefore, we model the general frequency response of the SMO films by a composition of a Drude term (index "0"), representing the response of the material in the THz domain, and a Lorentz-Drude term (index "1") for a resonance at an (angular) frequency of ω_1, leading to

$$\sigma = \frac{\epsilon_0 \omega_{p0}^2 \tau_0}{1 - i\tau_0\omega} + \frac{\epsilon_0 \omega_{p1}^2 \tau_1}{1 - i\tau_1(\omega - \omega_1^2/\omega)}, \tag{3}$$

with the plasma frequencies ω_{p0} and ω_{p1}, the scattering times τ_0 and τ_1, respectively. For vanishing oscillator strength $\epsilon_0 \omega_{p1}^2 \tau_1 \rightarrow 0$, the second term also vanishes and a pure Drude model is obtained.

To account for localization effects, the Drude model can be extended to the Drude-Smith model. The conductivity of nanometer-scale gold films can be described very well with the Drude-Smith model in the THz domain [15, 16]. The Drude-Smith model is a modification of the bare Drude model and includes non-isotropic backscattering of carriers,

$$\sigma = \frac{\epsilon_0 \omega_{p0}^2 \tau_0}{1 - i\tau_0\omega} \left(1 + \frac{c}{1 - i\tau_0\omega} \right), \tag{4}$$

where c describes the persistence of velocity [15]. The parameter c ranges from $c = -1$ for full carrier backscattering to $c = 0$ for isotropic backscattering. For $c = 0$, Eq. 4 becomes a Drude model.

For optical measurements, it is often imperative to also evaluate the complex refractive index, $\tilde{n} = n + i\kappa$, and the complex dielectric permittivity, $\epsilon = \epsilon' + i\epsilon''$. The dielectric permittivity is directly linked to the conductivity by

$$\epsilon = \epsilon_\infty - \frac{\sigma}{i\omega\epsilon_0}, \tag{5}$$

where ϵ_∞ is a constant, taking influences of resonances at frequencies much higher than the inspected frequency range into account. For ordinary materials, $\epsilon_\infty \geq 1$ in the visible, Terahertz, and microwave range. The complex refractive index is the square root of the dielectric permittivity, yielding

$$n, \kappa = \sqrt{\frac{|\epsilon| \pm \epsilon'}{2}} \tag{6}$$

where the "+" sign is for the refractive index, n, and the "−" sign yield the extinction coefficient, κ. In the DC limit ($\omega \rightarrow 0$), the Lorentz oscillator term for the conductance in Eq. 3 diminishes, proving that a simple Drude model is usually sufficient to describe the low frequency behavior. In the low frequency limit ($\omega \ll \tau_0^{-1}, \tau_1^{-1}$), the dielectric permittivity resulting from Eq. 3 becomes

$$\epsilon = \epsilon_\infty + \frac{\omega_{p1}^2}{\omega_1^2} - \frac{\omega_{p0}^2 \tau_0}{i\omega + \tau_0\omega^2}, \tag{7}$$

i.e., the Lorentz oscillator term yields an offset that is usually swallowed in $\epsilon_\infty' = \epsilon_\infty + \frac{\omega_{p1}^2}{\omega_1^2}$. It further explains why far away from any resonance, the dielectric
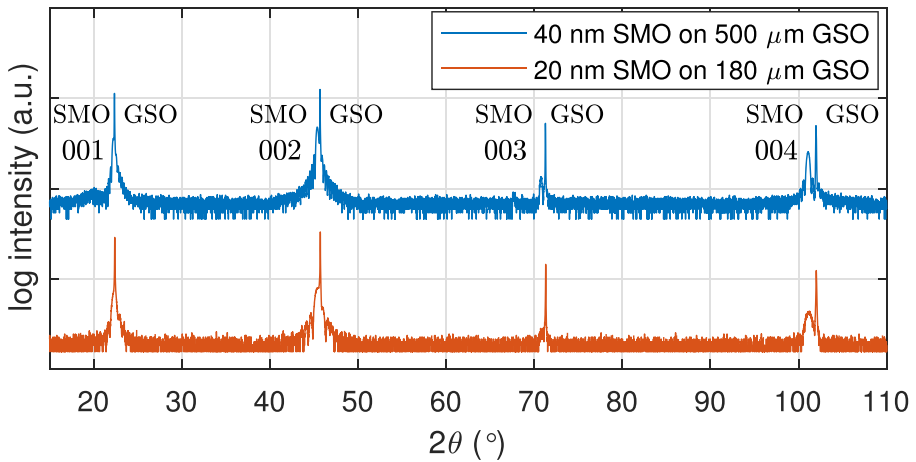
Fig. 1 Broad-range θ-2θ XRD pattern of 20-nm and 40-nm SMO films on GSO. Only GSO substrate peaks and 00l SMO peaks from phase-pure (00l)–oriented SMO films are observed

permittivity and, hence, the refractive index in the THz domain are usually larger than those in the optical domain. The Drude response survives and diverges for $\omega \rightarrow 0$, due to a constant, non-zero DC conductance, $\sigma_{DC} = \epsilon_0 \omega_{p0}^2 \tau_0$.

3 Crystal Structure and DC Electrical Properties

SMO thin films were epitaxially grown by pulsed laser deposition (PLD) onto $5 \times 5 \text{mm}^2$ (110)–oriented GSO substrates with a pseudocubic lattice constant of
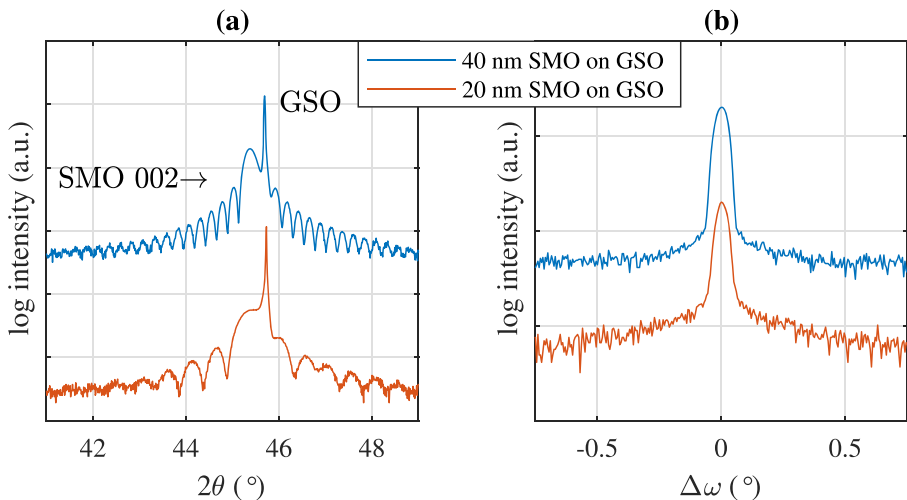

Fig. 2 X-ray diffraction of a 20-nm and a 40-nm SMO thin film on 0.5-mm- and 0.2-mm-thick GSO (110) substrates, respectively. (a) $2\theta - \theta$-scan of the SMO 002 reflection. The sharp peak on the right is accounted to the 220 reflection of the GSO substrate. (b) ω-scan (rocking curve) of the SMO 002 reflection

$a^* = 3.967$ Å. The details on the deposition conditions have been reported previously [7]. The structural quality of the SMO films was verified by X-ray diffraction (XRD) measurements, using a Rigaku SmartLab diffractometer in the parallel-beam geometry, equipped with a $2 \times$ Ge(220) monochromator.

Broad-range 2θ diffraction patterns of the prepared samples in Fig. 1 show only GSO substrate peaks and 00*l* SMO peaks from phase-pure (001)–oriented SMO films. The $\theta/2\theta$-scans near the 002 SMO peak of the films are shown in Fig. 2a. Due to the lattice mismatch of 0.2% to the GSO substrate and the resulting in-plane epitaxial compressive strain, the SMO films have a *c*-axis lattice parameter of 3.988 Å (3.990 Å) for the 20-nm- (40-nm)-thin film, determined by the Nelson-Riley extrapolation function. This value is slightly larger than the bulk value of $a_{SMO} = 3.974$ Å. The pronounced Laue oscillations near the 002 SMO peak indicate a high crystallinity of the films (Fig. 2a). The measured period of the Laue oscillations corresponds to a SMO film thickness of 19.88 ± 1.68 nm (40.43 ± 0.59 nm). The rocking curve (ω-scan) of the 002 SMO peak in Fig. 2b is narrow and shows a full width at half maximum (FWHM) of 0.05°, which is limited by the used X-ray beam monochromator. A similar small value has been measured for the 220 peak of the single-crystalline GSO substrate, indicating a low defect density in the SMO thin films and, therefore low mosaicity of the crystal structure.

The DC conductivity and electric properties of the SMO films were measured using a Physical Properties Measurement System (PPMS) by Quantum Design, supplemented with a current source 6221, nanovoltmeter 2182a, and matrix switch system 7001 by Keithley. The Hall voltage U_H was measured with the van der Pauw method, with gold electrodes sputtered on the sample corners. U_H was calculated by averaging the Hall voltages at positive and negative magnetic fields, in order to eliminate offsets in the measurement. The determined charge carrier density $n_e =$
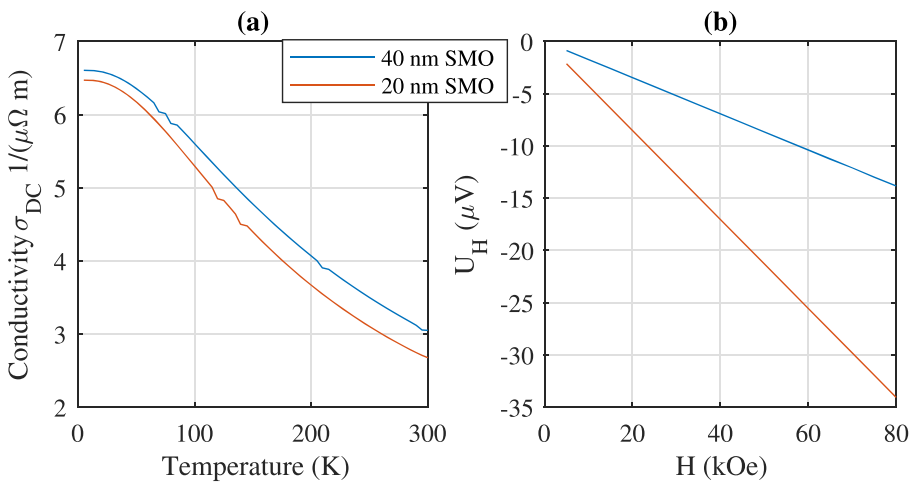

Fig. 3 (a) Temperature dependence of DC electric conductivity of the SMO thin films. (b) Hall voltage U_H versus magnetic field at 300 K. U_H was calculated by averaging the Hall voltages at positive and negative magnetic fields

3.67×10^{22} cm^{-3} is slightly higher than the theoretical value of 3.18×10^{22} cm^{-3}, which corresponds to 2 e$^-$ per formula unit coming from the $4d^2$ configuration of Mo^{4+}. The Hall mobility of $4.55 \frac{\text{cm}^2}{\text{Vs}}$ ($4.32 \frac{\text{cm}^2}{\text{Vs}}$ for 20 nm) is, as expected, lower than in d^1 metals such as SrVO$_3$ and SrNbO$_3$ [17, 18] (Fig. 3).

4 Results and Discussion

The THz characterization of SMO (performed on the 20-nm-thin film) was carried out with a pulsed 1550-nm time domain spectroscopy (TDS) system with a photo-conductive THz source and receiver from Menlo Systems/Fraunhofer Heinrich Hertz institute in a transmission configuration, similar to the one used in [19]. The system uses a 90-fs laser pulse at a repetition rate of 100 MHz, generating THz frequencies up to about 5 THz. The TDS measurement is repeated by mounting and unmounting the sample on a 4-mm aperture with a reference measurement in between to ensure reproducibility. The resulting conductivity is averaged over the number of repetitions. Fig. 4 shows the corresponding THz spectra of a single transmission. A Hamming window in time domain removes multiple reflections in the 0.2-mm substrate in the data analysis. The spectrum of the corresponding uncoated reference GSO substrate for the gold film measurement with a slightly thinner thickness is omitted in Fig. 4 for better readability. Due to absorption and reflection losses of the samples, useful data are only recorded up to about 2.2 THz. Data below 200 GHz were discarded as the error of TDS data increases towards DC. First, the refractive index of the GSO substrate, n_{GSO}, is determined from the time delay of the substrate. The imaginary part of the Fresnel transmission factors caused by the imaginary part of the refractive
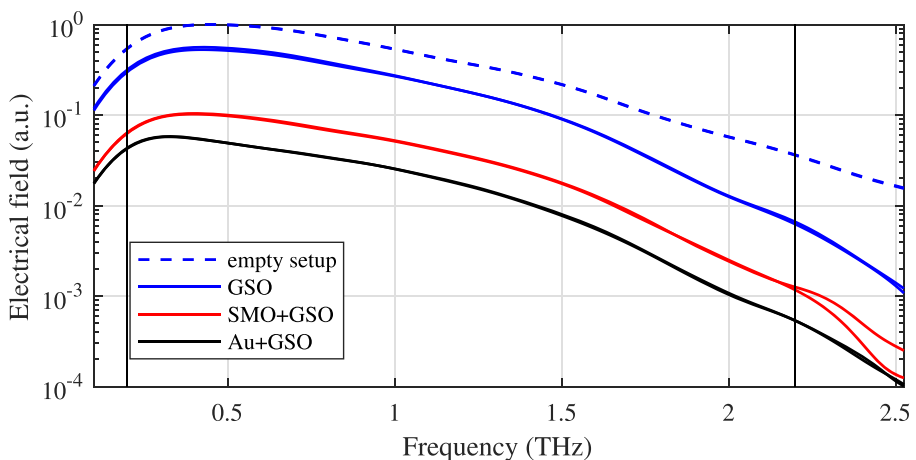

Fig. 4 Measured THz spectra of the empty setup (dashed blue lines), GSO substrate (solid blue lines), SMO film on GSO substrate (red lines), and gold film on GSO substrate (black lines). Each measurement is repeated twice by mounting and unmounting of the sample to evaluate systematic errors and repro-ducibility. The conductivity was extracted between 0.2 and 2.2 THz, where the repeated measurements show almost perfect coincidence with a relative error below 7%

index, κ_{GSO}, is marginal in comparison with the phase gain in the $d_{GSO} = 0.2$ mm substrate. The change in amplitude contains information about the reflection and the absorption coefficient, $\alpha = 4\pi\kappa/\lambda$, where λ is the (vacuum) THz wavelength. Second, the sample with the highly conductive SMO film is measured. The relative transmission, t, allows to calculate the conductivity with Eq. 1.

For a completion of the measurements on the upper end of the frequency range, we characterized SMO also in the visible spectrum. This measurement was performed on the 40-nm sample which had the same electric and structural properties as the sample used for the previous measurement, as can be seen from Figs. 2 and 3. In contrast to the THz measurements, power quantities instead of field quantities are measured. An Agilent Cary 7000 spectrometer is used to measure the normal power transmission T and reflexion R under an angle of $\pm 6°$. The refractive index is calculated numerically, taking the refractive index of the GSO substrate into account. Dividing the power transmitted through the thin film and substrate P_{fs} through the power transmitted through the substrate P_s yields the relative transmitted power $T = P_{fs}/P_s$.

The refractive index of the GSO substrate calculates to $n = 4.7 \pm 0.3$ and $\kappa = 0.10 \pm 0.08$ from 0.2 up to 2.2 THz and $n = 2.1 \pm 0.1$ in the visible part of the electromagnetic spectrum (shown in Fig. 5).

In the THz domain, both the real and imaginary part of the refractive index of SMO and Au are large as compared to the GSO substrate, due to the high conductivity of the materials. In the visible part of the spectrum, GSO features a vanishing imaginary part of the refractive index; i.e., it features a very low loss that is at the resolution limit of the system. Similarly, the extinction coefficient, κ, of SMO is about 4 orders of magnitude smaller in the visible and decreases with a power law $\propto f^{-0.5}$ with increasing frequency. For the 40-nm film, the absorption, A is about 26% at a wavelength of 800 nm and decreases to 16% at 400 nm. Therefore, SMO qualifies
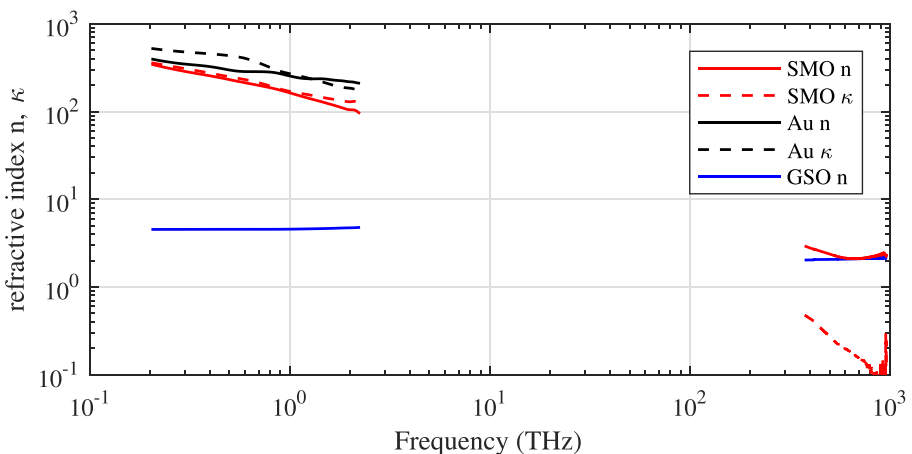

Fig. 5 Real (imaginary) part of the refractive index, n (κ), in the THz and visible part of the spectrum for the SMO and Au thin film (red and black) and the GSO substrate (blue)
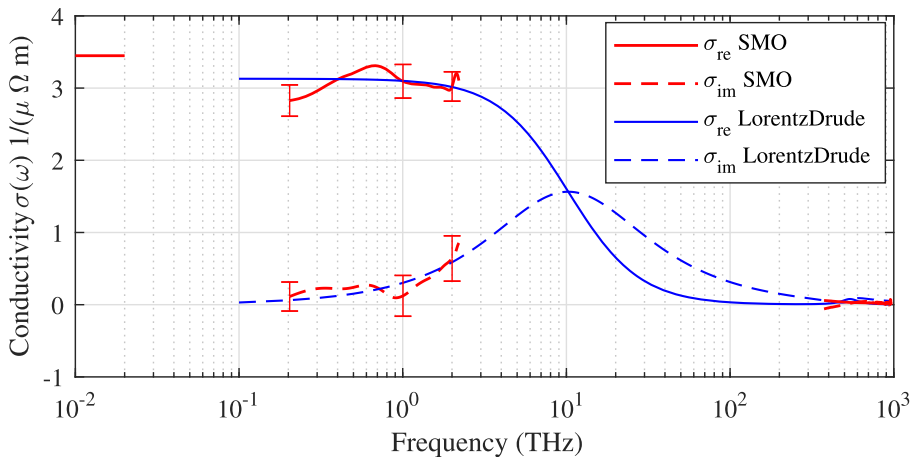
Fig. 6 Real (solid line) and imaginary part (dashed line) of the conductivity of SMO in the THz and visible part of the spectrum. The real part of the conductivity is extended by microwave data from ref. [7] where a SMO thin film with comparable physical properties in a coplanar waveguide geometry was used for measuring the AC conductivity. The Lorentz-Drude model is fitted to the THz and visible spectrum (blue curves)

well for transparent electrodes in the visible domain. The real part of the refractive index $n \approx 2.1 \dots 2.9$ of GSO and SMO is very similar in the visible frequency range.

Figure 6 shows the extracted conductivity for SMO in the THz and visible part of the spectrum. Additionally, the graph includes data from the GHz range for a SMO thin film [7]. The THz conductivity on the low frequency end and the GHz conductivity show very good agreement, with only about 10% higher conductivity of the film in the GHz range. As the film measured in the GHz regime had a thickness of about 150 nm, it can be concluded that confinement effects caused by ultra low film thickness play only a minor role [8]. There is also very good agreement of the THz conductivity $\sigma = 3.1 \pm 0.5 \frac{1}{\mu\Omega m}$ and the DC conductivity $\sigma_{DC} = 2.7 \frac{1}{\mu\Omega m}$ for the 20-nm SMO film (cf. Fig. 3).

In order to extract the material parameters, the complex conductance was fitted with Eq. 3. At first, the Drude model Eq. 2 is fitted to the THz data only where the Lorentz term of the conductance is negligible and shows good agreement. The extracted parameters of the SMO film are a plasma frequency of $\omega_{p0} = 2\pi \cdot (760 \pm 100 \text{ THz})$ and a scattering time of $\tau_0 = 15.5 \pm 4$ fs. A fit to the Drude-Smith model Eq. 4 results in the same parameters as the Drude model with $c = 0$, indicating no localization effects.

Subsequently, the complete data set of THz and visible conductivity is fitted with the full Lorentz-Drude model of Eq. 3, while keeping the parameters obtained from the THz fit constant. This yields for the resonance frequency $\omega_1 = 2\pi \cdot (540 \pm 30 \text{ THz})$, $\omega_{p1} = 2\pi \cdot (470 \pm 100 \text{ THz})$, and $\tau_1 = 1 \pm 0.7$ fs. As no resonance is observed in the measured visible spectrum, the amplitude $\epsilon_0 \tau_1 \omega_{p1}^2$ of the fitted Lorentz oscillator in the visible domain is two orders of magnitude smaller as the resonator of the pure Drude model. Therefore, the fits of the Lorentz contribution

also show large errors. Despite its small amplitude, the Lorentz oscillator allows for a better fit in the visible domain and a comparison with literature.

The Drude term is in agreement with the study of Wells et al. for a Lorentz-Drude fit to the visible and near infrared (NIR) part of the spectrum of a 100-nm SMO thin film on a SrTiO$_3$ substrate with $\omega_{p0} = 2\pi \cdot 890$ THz ($\hat{=}3.68$ eV) and $\tau_0 = 12.7$ fs ($\hat{=}0.325$ eV) [11]. The DC conductivity of the Drude model in ref. [11] is therefore $\sigma_{\omega \to 0} = \epsilon_0 \omega_{p0}^2 \tau = 3.5 \frac{1}{\mu\Omega\,\text{m}}$. However, the measured DC conductivity of the SMO film in ref. [11] is $\sigma_{DC} = 1 \frac{1}{\mu\Omega\text{m}}$, indicating a different defect structure as compared to the films reported in this paper.

Furthermore, the Lorentz oscillator parameters differ. Wells et al. reported values of $\omega_{p1} = 2\pi \cdot 848$ THz ($\hat{=}\sqrt{3.65} \times 1.8345$ eV), $\omega_1 = 2\pi \cdot 444$ THz ($\hat{=}1.8345$ eV), and $\tau_1 = 2$ fs ($\hat{=}2.065$ eV), i.e., a 1.6 times higher resonance frequency than found in this study. In a review article, Doiron, Mota, Wells et al. reported values of $\tau_0 = 11.8$ fs, $\omega_1 = 2\pi \cdot 428$ THz ($\hat{=}1.77$ eV) and, $\tau_1 = 3.9$ fs ($\hat{=}1.06$ eV) [20]. The different values of the additional Lorentz oscillator can be accounted to the much thicker 100-nm SMO layer used in the mentioned study by Wells et al. that shows a clear resonance in the spectroscopic measurements [11]. For a 40-nm SMO thin film, no resonance is observed in the visible part of the spectrum both in this study (shown in Fig. 6 and in ref. [11]).

The THz conductivity of a sputtered Au film (20 nm thickness) on GSO is shown in Fig. 7. The fitted Drude-Smith model with the parameters $\omega_p = 2\pi \cdot (2000 \pm 300$ THz$)$, $\tau = 13.4 \pm 5$ fs, and $c = -0.6 \pm 0.1$ shows good agreement with literature [15, 21]. The negative c parameter indicates a reduced film quality which fits to the fact that the film was sputtered at room temperature and is non-crystalline. Furthermore, the absolute conductivity is also smaller than the bulk conductivity of $45 \frac{1}{\mu\Omega\text{m}}$ while the recorded real part of the conductance of $\sigma_{re} = 8.0 \pm 1.3 \frac{1}{\mu\Omega\text{m}}$ is in excellent
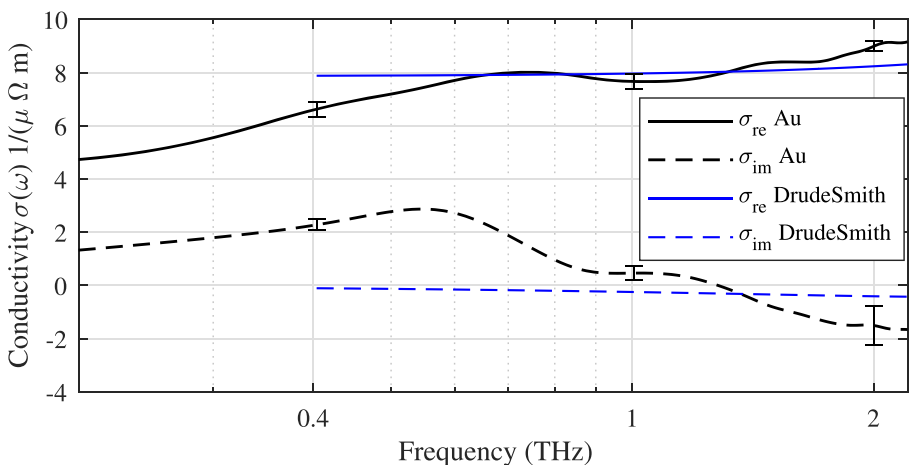

Fig. 7 Real and imaginary conductivity (solid and dashed red line) of Au in the THz and visible part of the spectrum. The Drude model is fitted to the THz spectrum

agreement with that of high-quality films from the literature with $\sigma_{re} = 8\frac{1}{\mu\Omega m}$ for 12 nm Au [15]. A zero-crossing of the imaginary part, σ_{im}, indicates a localization of the charge carriers and is also observed for an even thinner, 6-nm Au film in literature [15]. We note, however, that the error of σ_{im} increases towards 2.2 THz due to the lower signal to noise ratio of the transmission through the substrate. The decrease of conductivity below 400 GHz is not expected and can be accounted to spatial non-uniformity and imaging aberrations by the sample aperture, as the spot-size of the THz beam is larger at lower frequencies.

5 Conclusion and Outlook

The AC conductivity of high-quality, epitaxial $SrMoO_3$ (SMO) thin films has been characterized in the THz and visible part of the electromagnetic spectrum, completed by data from the microwave range and DC values. SMO features a conductivity comparable to those of the most conductive metals, even for films as thin as 20 nm. The conductance of SMO is only about 2.3 times smaller than that of a sputtered gold thin film of same thickness, about 12 times smaller than that of the literature value of bulk gold, and about 30% higher than that of the bulk value of titanium $(2.5\frac{1}{\mu\Omega m})$. An integration of highly conducting SMO electrodes with structurally compatible perovskite materials with tunable band gap (e.g. $SrTiO_3$ and $Ba_xSr_{1-x}TiO_3$) potentially allows all-oxide devices in the THz range.

References

1. A. Radetinac, J. Ziegler, M. Vafaee, L. Alff, P. Komissinskiy, Journal of Crystal Growth **463**, 134 (2017). https://doi.org/10.1016/j.jcrysgro.2017.02.015.
2. P. Salg, D. Walk, L. Zeinar, A. Radetinac, L. Molina-Luna, A. Zintler, R. Jakoby, H. Maune, P. Komissinskiy, L. Alff, APL Materials **7**(5), 051107 (2019). https://doi.org/10.1063/1.5094855.
3. R. Singh, A.K. Azad, Q.X. Jia, A.J. Taylor, H.T. Chen, Optics Letters **36**(7), 1230 (2011). https://doi.org/10.1364/OL.36.001230.
4. H.T. Chen, H. Yang, R. Singh, J.F. O'Hara, A.K. Azad, S.A. Trugman, Q.X. Jia, A.J. Taylor, Phys. Rev. Lett. **105**, 247402 (2010). https://doi.org/10.1103/PhysRevLett.105.247402.
5. A. Radetinac, K.S. Takahashi, L. Alff, M. Kawasaki, Y. Tokura, Applied Physics Express **3**(7), 073003 (2010). https://doi.org/10.1143/apex.3.073003.

6. I. Nagai, N. Shirakawa, S.i. Ikeda, R. Iwasaki, H. Nishimura, M. Kosaka, Applied Physics Letters **87**(2), 024105 (2005). https://doi.org/10.1063/1.1992671.
7. A. Radetinac, A. Mani, S. Melnyk, M. Nikfalazar, J. Ziegler, Y. Zheng, R. Jakoby, L. Alff, P. Komissinskiy, Applied Physics Letters **105**(11), 114108 (2014). https://doi.org/10.1063/1.4896339.
8. A. Radetinac, J. Zimmermann, K. Hoyer, H. Zhang, P. Komissinskiy, L. Alff, Journal of Applied Physics **119**(5), 055302 (2016). https://doi.org/10.1063/1.4940969.
9. H. Mizoguchi, N. Kitamura, K. Fukumi, T. Mihara, J. Nishii, M. Nakamura, N. Kikuchi, H. Hosono, H. Kawazoe, Journal of Applied Physics **87**(9), 4617 (2000). https://doi.org/10.1063/1.373111.
10. H. Wadati, J. Mravlje, K. Yoshimatsu, H. Kumigashira, M. Oshima, T. Sugiyama, E. Ikenaga, A. Fujimori, A. Georges, A. Radetinac, K.S. Takahashi, M. Kawasaki, Y. Tokura, Phys. Rev. B **90**, 205131 (2014). https://doi.org/10.1103/PhysRevB.90.205131.
11. M.P. Wells, B. Zou, B.G. Doiron, R. Kilmurray, A.P. Mihai, R.F.M. Oulton, P. Gubeljak, K.L. Ormandy, G. Mallia, N.M. Harrison, L.F. Cohen, S.A. Maier, N.M. Alford, P.K. Petrov, Advanced Optical Materials **5**(22), 1700622 (2017). https://doi.org/10.1002/adom.201700622.
12. M. Tinkham, Physical Review **104**(3), 845 (1956). https://doi.org/10.1103/PhysRev.104.845.
13. P. Jepsen, D. Cooke, M. Koch, Laser a. Photonics Reviews **5**(1), 124 (2011). https://doi.org/10.1002/lpor.201000011.
14. J. Neu, C.A. Schmuttenmaer, Journal of Applied Physics **124**(23), 231101 (2018). https://doi.org/10.1063/1.5047659.
15. M. Walther, D.G. Cooke, C. Sherstan, M. Hajar, M.R. Freeman, F.A. Hegmann, Physical Review B **76**(12), 125408 (2007). https://doi.org/10.1103/PhysRevB.76.125408.
16. R. Ulbricht, E. Hendry, J. Shan, T.F. Heinz, M. Bonn, Reviews of Modern Physics **83**(2), 543 (2011). https://doi.org/10.1103/RevModPhys.83.543.
17. L. Zhang, Y. Zhou, L. Guo, W. Zhao, A. Barnes, H.T. Zhang, C. Eaton, Y. Zheng, M. Brahlek, H.F. Haneef, N.J. Podraza, M.H.W. Chan, V. Gopalan, K.M. Rabe, R. Engel-Herbert, Nature Mater **15**(2), 204 (2016). https://doi.org/10.1038/nmat4493.
18. D. Oka, Y. Hirose, S. Nakao, T. Fukumura, T. Hasegawa, Phys. Rev. B **92**, 205102 (2015). https://doi.org/10.1103/PhysRevB.92.205102.
19. M. Méndez Aller, A. Abdul-Munaim, D. Watson, S. Preu, Sensors **18**(7), 2087 (2018). https://doi.org/10.3390/s18072087.
20. B. Doiron, M. Mota, M.P. Wells, R. Bower, A. Mihai, Y. Li, L.F. Cohen, N.M. Alford, P.K. Petrov, R.F. Oulton, S.A. Maier, ACS Photonics **6**(2), 240 (2019). https://doi.org/10.1021/acsphotonics.8b01369.
21. N. Laman, D. Grischkowsky, Applied Physics Letters **93**(5), 51105 (2008). https://doi.org/10.1063/1.2968308.